Variability of visual field maps in human early extrastriate cortex challenges the canonical model of organization of V2 and V3

Fernanda L. Ribeiro[a,b*], Ashley York[a,b], Elizabeth Zavitz[c,d], Steffen Bollmann[e], Marcello G. P. Rosa[c,d¶], Alexander M. Puckett[a,b¶]

Affiliations:

[a] School of Psychology, The University of Queensland; Brisbane QLD 4072; Australia

[b] Queensland Brain Institute, The University of Queensland; Brisbane QLD 4072; Australia

[c] Department of Physiology, Monash University; Clayton VIC 3800; Australia

[d] Neuroscience Program, Biomedicine Discovery Institute; Monash University; Clayton VIC 3800; Australia

[e] School of Information Technology and Electrical Engineering, The University of Queensland; Brisbane QLD 4072; Australia

[¶] Joint senior authors

* Corresponding author: fernanda.ribeiro@uq.edu.au

Abstract

Visual field maps in human early extrastriate areas (V2 and V3) are traditionally thought to form mirror-image representations which surround the primary visual cortex (V1). According to this scheme, V2 and V3 form nearly symmetrical halves with respect to the calcarine sulcus, with the dorsal halves representing the lower contralateral quadrants, and the ventral halves representing the upper contralateral quadrants. This arrangement is considered to be consistent across individuals, and thus predictable with reasonable accuracy using templates. However, data that deviate from this expected pattern have been observed, but mainly treated as artifactual. Here we systematically investigate individual variability in the visual field maps of human early visual cortex using the large-scale 7T Human Connectome Project (HCP) retinotopy dataset. Our results demonstrate substantial and principled inter-individual variability in early visual retinotopy. Visual field representation in the dorsal portions of V2 and V3 were more variable than their ventral counterparts, including substantial departures from the expected mirror-symmetrical patterns. Surprisingly, only one-third of individuals had maps that conformed to the expected pattern. In addition, retinotopic maps in the left hemisphere were more variable than those in the right hemisphere. Our findings challenge the current view that inter-individual variability in early extrastriate cortex is negligible, and that the dorsal portions of V2 and V3 are roughly mirror images of their ventral counterparts.

Keywords

human connectome project, retinotopy, high-resolution fMRI, 7T, vision, hemispheric differences, V3

Introduction

Non-invasive imaging has been instrumental in mapping the topographic organization of human visual cortex (Wandell and Winawer, 2010). The visual field maps in early visual areas (V1, V2, and V3) have been reported to be remarkably consistent across people, and predictable with reasonable accuracy using a template (Benson et al., 2014, 2012; Schira et al., 2010). While V1 contains a complete, first-order (continuous) representation of the contralateral visual hemifield, areas V2 and V3 form second-order (discontinuous) representations (Rosa, 2002). In these areas, a field discontinuity near the horizontal meridian splits the maps into upper and lower field representations that are only connected at the foveal confluence (Figure 1a,b). Accordingly, in parcellation schemes (Glasser et al., 2016; Wang et al., 2015), early visual areas form concentric bands, arranged in nearly symmetrical halves with respect to the calcarine sulcus. These bands, each containing the representation of a contralateral visual field quadrant, are referred to as the dorsal and ventral portions of V2 and V3 (Figure 1a). However, observations originating in several laboratories has indicated departures from this pattern, particularly in the dorsal region (Allen et al., 2021; Arcaro and Kastner, 2015; Benson and Winawer, 2018; Van Essen and Glasser, 2018). Even so, small-sized datasets, variability in acquisition sites and protocols, and methodological constraints have limited the investigation of this variability. As a result, no consensus exists about deviations from the canonical mirror-symmetrical organization of V2 and V3.

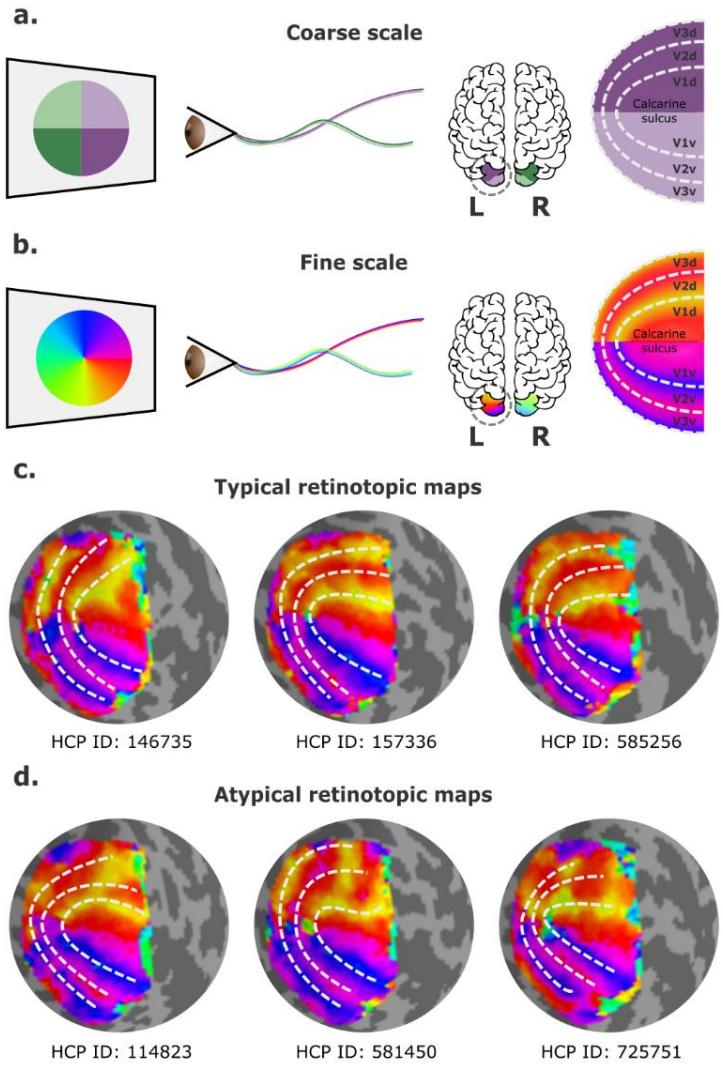

Figure 1 – Visual field mapping in the human early visual cortex. a, Coarse scale visual field mapping in the early visual cortex. The left (L) hemisphere maps the right visual field, and the right (R) hemisphere maps the left visual field. The dorsal portion of early visual areas maps the lower hemifield, and the ventral portion the upper field. **b,** Fine scale visual field mapping with visual field maps represented in polar angles (0-360º). The vertical (90º or 270º) and horizontal meridians (0º for the left and 180º for the right hemispheres) delineate boundaries between visual areas. **c,** Three "typical" polar angle maps, obtained from the left hemispheres of three individuals in the HCP retinotopy dataset, which conform to the traditional model. **d,** Three polar angle maps that deviate from this pattern, obtained from left hemispheres of three other individuals in the HCP retinotopy dataset. In the latter, the isopolar bands representing the anterior borders of dorsal V3 (V3d) and dorsal V2 (V2d) do not follow the proposed borders of V2 and V3 (dashed lines).

In humans, empirical visual field mapping using functional MRI (fMRI) is the primary means of delineating precise visual area boundaries in individuals. Visual field maps are typically defined in polar coordinates, resulting in two maps: one representing polar angle (or clock position) and the other eccentricity (or distance away from the fixation point) (Wandell and Winawer, 2010). In primates, isoangle bands representing the vertical and the horizontal meridians are thought to delineate boundaries between V1 and V2, V2 and V3, and V3 and higher-order visual areas (Figure 1b). Particularly, in human probabilistic maps, boundaries between the dorsal portions of early visual areas are roughly mirror images of their ventral counterparts (Figure 1c). Nevertheless, boundaries that deviate from the expected ones exist, but these have been mainly treated as artifactual, with researchers often overlooking the irregularities by simply drawing the boundaries to resemble that of a typical map as best as possible (Figure 1d). Here, it may be important to remark that the border between the dorsal parts of V2 and V3 is well known to be variable in other mammals, and that it typically does not coincide with the representation of the horizontal meridian (see Rosa and Manger, 2005 for review).

Although previous reports of individual variability in the dorsal portion of human early visual cortex were primarily anecdotal (Allen et al., 2021; Arcaro and Kastner, 2015; Benson and Winawer, 2018; Van Essen and Glasser, 2018), a recently developed deep learning model predicts that individual variability in retinotopy exists, and that this is correlated with variations in gross anatomy (e.g., the pattern of sulci and gyri) (Ribeiro et al., 2021). Moreover, studies modelling the formation of retinotopic maps in non-human primates also indicate that different variants could develop based on application of similar rules (Yu et al., 2020).

Motivated by these findings, here we systematically investigate individual variability in visual field maps of human early visual cortex using a recently released, large-scale dataset: the 181 participants, 7T Human Connectome Project (HCP) retinotopy dataset (Benson et al., 2018). Our aims were to quantify the level of individual variability throughout early visual cortex (V1-V3) and to determine whether there are common modes of retinotopic organization that differ from the established view (i.e., whether individual retinotopic maps differ from a template in similar ways). Our results challenge the current view that individual differences in retinotopic organization reflect experimental artifacts that may be dismissed for practical purposes. In particular, they demonstrate that the dorsal portions of human early visual areas are more heterogeneous than previously acknowledged.

Materials and Methods

Dataset

We used the Human Connectome Project (HCP) 7T Retinotopy dataset (Benson et al., 2018) to investigate individual variability in retinotopic maps of human early visual cortex. This dataset consists of high-resolution functional retinotopic mapping and structural data from 181 participants (109 females, age 22-35) with normal or corrected-to-normal visual acuity. Participant recruitment and data collection were led by Washington University and the University of Minnesota. The Institutional Review Board (IRB) at Washington University approved all experimental procedures (IRB number 201204036; “Mapping the Human Connectome: Structure, Function, and Heritability”), and all participants provided written informed consent before data

collection (Van Essen et al., 2013). Additionally, the acquisition protocol has been described in previous work (Benson et al., 2018; Van Essen et al., 2013).

Structural data were acquired at 0.7 mm isotropic resolution in a customized Siemens 3T Connectome scanner (Van Essen et al., 2013). Briefly, cortical surfaces were reconstructed from T1w structural images using FreeSurfer and aligned to the 32k fs_LR standard surface space. This standard 32k fs_LR cortical surface consists of 32,492 vertices sparsely connected, forming triangular faces. Functional data were later aligned with this standard surface space.

Functional retinotopic mapping data were acquired using a Siemens 7T Magnetom scanner at 1.6 mm isotropic resolution and 1 s TR. Data were preprocessed following the HCP pipeline (Glasser et al., 2013), which included correction for head motion and EPI spatial distortion, alignment of the fMRI data with the HCP standard surface space, and denoising for spatially specific structured noise. Retinotopic mapping stimuli comprised rotating wedges, expanding and contracting rings, and bars of different orientations moving across different directions in the visual field. A population receptive field (pRF) modeling procedure was then used to reconstruct visual field maps (Benson et al., 2018; Dumoulin and Wandell, 2008; Kay et al., 2013), which encompasses estimating the spatial preference of cortical surface vertices to different locations of the visual field (i.e., its receptive field) defined in polar coordinates – for more, see Benson et al, (2018). Hence, polar angle maps are retinotopic maps reflecting the polar angle (angle relative to the horizontal vertical meridian) in the visual field to which a vertex is most responsive, while eccentricity maps reflect the distance from the center of the visual field (i.e., the fixation point). The combination of a polar angle map and an eccentricity map completely specifies a map of the visual field.

Region of Interest

Early visual areas were defined by a surface-based probabilistic atlas (Wang et al., 2015). This probabilistic atlas includes the dorsal and ventral portions of V1, V2 and V3, not including the foveal confluence. For the clustering analysis, we slightly modified the atlas by extending the dorsal border of V3 and including V1/V2/V3 foveal confluence (Schira et al., 2009), in line with our previous work (Ribeiro et al., 2021).

Individual variability

We determined individual variability in visual field maps to quantify how variable these maps were across visual areas (V1, V2, and V3), portions (dorsal and ventral), and hemispheres (left and right) in human early visual cortex. First, we computed the average retinotopic maps across all 181 individuals from the HCP retinotopy dataset for both left and right hemispheres. Then, we iteratively calculated the vertex-wise difference between an individual's retinotopic map and the average map. The difference between two angles is given by:

$$\text{MIN}\left(\left|\widehat{\boldsymbol{\theta}} - \boldsymbol{\theta}\right|, \left|\widehat{\boldsymbol{\theta}} - \boldsymbol{\theta} + \mathbf{2}\boldsymbol{\pi}\right|, \left|\widehat{\boldsymbol{\theta}} - \boldsymbol{\theta} - \mathbf{2}\boldsymbol{\pi}\right|\right) \quad (1)$$

for $0 < \theta < 2\pi$.

Finally, vertex-wise difference scores were averaged over vertices in the range of 1-8º of eccentricity within the dorsal and ventral portions of early visual areas, resulting in one scalar value per individual per visual area, which we refer to as the individual variability. The eccentricity mask was defined using the group-average eccentricity map. This range of eccentricity values was chosen because, in the original population receptive field mapping experiment of the HCP, the visual stimulus extended to 8° of eccentricity (Benson et al., 2018). Additionally, due to the inherent difficulty in mapping

168 the foveal confluence (Schira et al., 2009), we constrained our comparison to
169 eccentricity values above 1°. According to studies in non-human primates, this
170 corresponds approximately to half of the expected extent of V1, V2 and V3 (Gattass
171 et al., 1988, 1981).

172 ***Linear mixed-effects model***

173 We determined whether there were main effects and interactions of hemispheres (left,
174 right), visual areas (V1, V2, V3), and portions (dorsal, ventral) on individual variability
175 of retinotopic maps using linear mixed-effect (LME) models. Standard ANOVAs and t-
176 tests assume statistical independence of individuals' data (Yu et al., 2022), which is
177 often not the case. For example, the 7T HCP retinotopy dataset includes data from 50
178 monozygotic and 34 dizygotic twins, totaling 168 individuals out of 181. Therefore, to
179 meet the statistical independence criterion, many data points would have to be
180 disregarded for standard statistical inference. However, LME models allow us to take
181 full advantage of the dataset by explicitly modeling cluster-specific means (random
182 intercepts). Indeed, individual variability from different visual areas is naturally
183 clustered by individuals (Magezi, 2015). Therefore, using this statistical model, we can
184 appropriately model individual-specific effects (Magezi, 2015; Yu et al., 2022).

185 In our linear mixed effect model, the dependent variable is the individual variability (Y),
186 which is modeled as a function of the fixed effects (β) of three factors (x) and their
187 interactions. These three factors are: hemisphere, visual area, and portion.
188 Additionally, we also consider the random effects (γ_i) associated with the individual (i
189 = 1, …, 181), and the random effects of each factor nested within the individual (γ_{ij},
190 with j = 1, 2, and 3). This model is expressed as:

191 $$Y_i = \beta_0 + \sum_{j=1}^{3} \beta_j x_j + \beta_{12} x_1 x_2 + \beta_{13} x_1 x_3 + \beta_{23} x_2 x_3 + \beta_{123} x_1 x_2 x_3 + \sum_{j=1}^{3} \gamma_{ij} + \gamma_i + \varepsilon_i$$

192 where β_0 is the intercept and ε is the residual random error. We built two separate
193 models for individual variability associated with polar angle and eccentricity maps
194 using Jamovi ("The jamovi project (2021)," n.d.).

195 ***Clusters of spatial organization***

196 Lastly, we performed an exploratory clustering analysis to determine whether
197 retinotopic maps differ from the average map in similar ways, particularly in the dorsal
198 portion of early visual cortex. Specifically, we investigated the spatial overlap between
199 retinotopic maps as an unambiguous indicator of the similarity between two maps.
200 First, to obtain such a measure of the spatial overlap, the continuous polar angle maps
201 were converted into discrete maps, such that each vertex was categorized into one
202 out of four possible labels:

203 $$\theta_{discrete} = \begin{cases} 0°, for\ 0° \leq \theta_{continuous} \leq 45° \\ 90°, for\ 45° < \theta_{continuous} \leq 180° \\ 270°, for\ 180° \leq \theta_{continuous} < 315° \\ 360°, for\ 315° \leq \theta_{continuous} < 360° \end{cases}$$

204 these categories were chosen because they highlight the location of visual area
205 boundaries. Discrete eccentricity maps were determined by:

206 $$\theta_{discrete} = \begin{cases} 0°, for\ 0° \leq \theta_{continuous} \leq 2° \\ 2°, for\ 2° < \theta_{continuous} \leq 4° \\ 4°, for\ 4° < \theta_{continuous} \leq 6° \\ 6°, for\ 6° < \theta_{continuous} \end{cases}$$

207 Next, the spatial overlap between discrete maps from all possible pairs of individuals
208 was estimated using the Jaccard similarity coefficient (Levandowsky and Winter, 1971;
209 Taha and Hanbury, 2015). The Jaccard index estimates similarity between two maps

by taking the size of the intersection (in number of vertices) divided by the size of the union of two label sets. Hence, the Jaccard score ranges from 0 to 1; the closer to 1 the score is, the more similar the two maps are. For our data and each pair of individuals, the Jaccard index is determined from the two possible individuals' combinations (i.e., individual 1 *vs.* individual 2 and individual 2 *vs.* individual 1) since the order of the maps determines which map is the reference one. For each combination, we estimated the Jaccard index for each label, and their weighted average was determined using the number of labels' instances in the reference map to account for label imbalance. Then, these two estimates were averaged, resulting in one estimate of the spatial overlap between two individuals' discrete retinotopic maps.

To assess whether inter-individual differences fell into stereotyped patterns, we applied a spectral clustering algorithm from Scikit-learn (Abraham et al., 2014; Pedregosa et al., 2011). This algorithm operates on the low-dimensional embedding of the affinity matrix (our Jaccard index-based similarity matrix), followed by K-means clustering of the components of the eigenvectors in the low-dimensional space. This low dimensional space is determined by selecting the most relevant eigenvectors of the graph Laplacian of the affinity matrix, of which corresponding eigenvalues reflect important properties of the affinity matrix that can be used to partition it (Luxburg, 2007). In implementing the spectral clustering algorithm, we set the number of clusters to 6 and fixed the random state for replication purposes. We selected this number of clusters as there are at least five different models of third-tier visual cortex organization in non-human primates (Angelucci and Rosa, 2015), with a sixth cluster intended to capture noisy or unclear retinotopic organization. After clustering, we computed each cluster's mean map by averaging the continuous retinotopic maps across individuals within each cluster.

Data and code availability

The data used in this study is publicly available at BALSA (https://balsa.wustl.edu/study/show/9Zkk). All accompanying Python source code will be available upon publication on GitHub.

Results

We defined an individual variability metric to quantify how variable visual field maps are across visual areas (V1, V2, and V3), portions (dorsal and ventral), and hemispheres (left and right) in human early visual cortex. First, we computed the average visual field maps across all 181 individuals from the HCP retinotopy dataset for both left and right hemispheres. Then, we iteratively calculated the difference between an individual's visual field map and the average map. Finally, these differences were averaged over all vertices within the dorsal and ventral portions of early visual areas, resulting in one scalar value per individual per visual area, which is our individual variability metric. Figure 2 shows the distribution of individual variability scores across all participants.

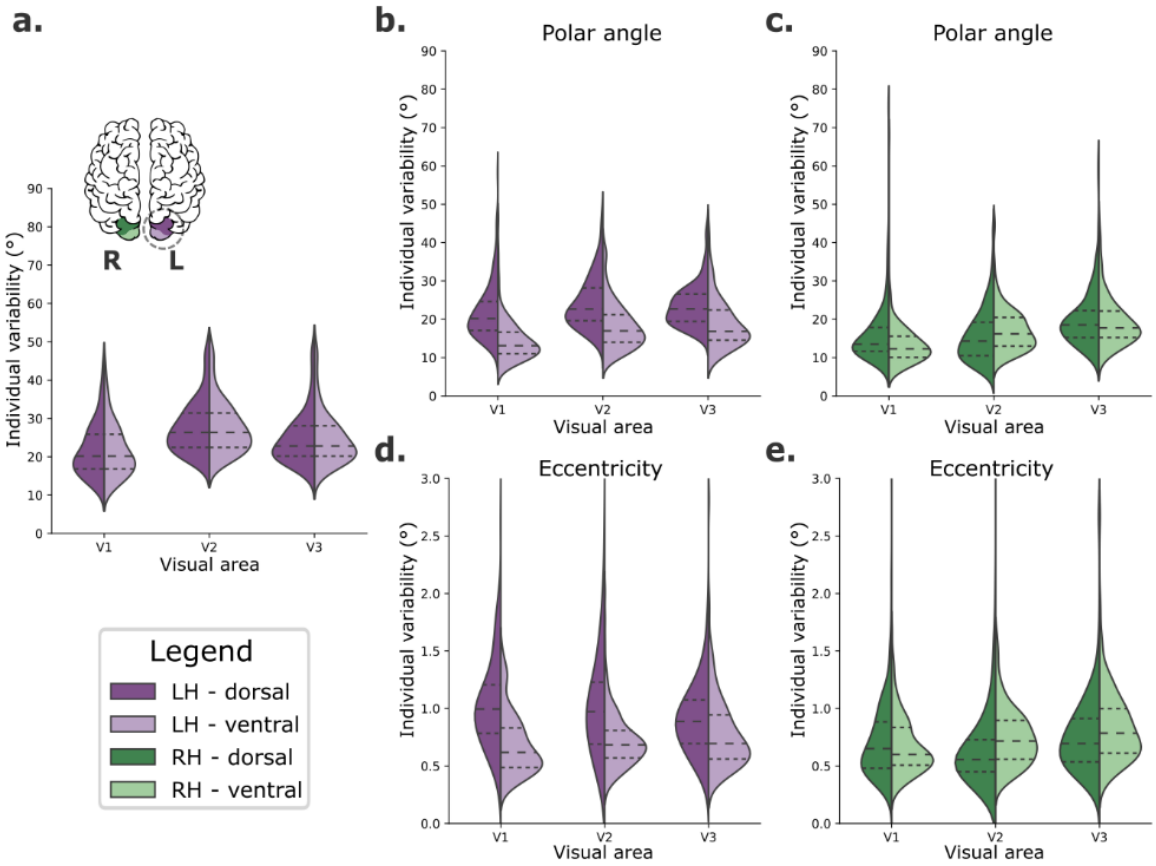

Figure 2 – Individual variability in visual field maps of early visual areas. a, Hypothetical diagram of symmetrical distributions of individual variability across visual areas. Empirical distributions of individual variability of polar angle (**b** and **c**) and eccentricity (**d** and **e**) maps for both dorsal (dark shades) and ventral (lighter shades) portions of early visual areas in left (purple) and right (green) hemispheres.

We built a linear mixed effect model (Yu et al., 2022) to test the fixed effects of hemispheres, visual areas, and portions on individual variability of polar angle (Table 1) and eccentricity (Table 2) maps. Table 1 shows statistically significant main effects of all factors on individual variability of polar angle maps. Specifically, polar angle maps of the left hemisphere show higher individual variability than those found in the right hemisphere (mean difference = 3.35, $p<.001$). The dorsal portions of early visual areas are also more variable than the ventral portions (mean difference = 3.30, $p<.001$). Finally, post-hoc comparisons of visual areas indicated that V3 has higher

264 individual variability than V2 (mean difference = 1.60, p<.001) and V1 (mean difference
265 = 3.99, p<.001); V2 also has higher individual variability than V1 (mean difference =
266 2.38, p<.001). For brevity, we only show the main effects in Table 1, although we also
267 found statistically significant interactions. Briefly, each visual area in the left
268 hemisphere has significantly higher individual variability than its analogous area in the
269 right hemisphere. In addition, the dorsal portion of each visual area of the left
270 hemisphere is significantly more variable than its dorsal analogue in the right
271 hemisphere and the ventral analogue of both the left and right hemispheres (for more,
272 see the Supplementary Material). These findings suggest that individual variability in
273 polar angle representations varies across hemispheres, visual areas, and according
274 to dorsal/ventral locations.

Table 1 - Fixed effects parameter estimates for the linear mixed effect model of individual variability of polar angle maps. SE – standard error; CI – confidence interval.

Polar angle								
				95% CI				
Names	**Effect**	**Estimate**	**SE**	**Lower**	**Upper**	**df**	**t**	**p**
Intercept	Intercept	18.58	0.30	17.99	19.17	180	61.86	<.001
Hemisphere	RH-LH	-3.35	0.32	-3.97	-2.72	181	-10.47	<.001
Visual area (1)	V2-V1	2.38	0.29	1.81	2.95	210	8.21	<.001
Visual area (2)	V3-V1	3.99	0.32	3.36	4.61	187	12.54	<.001
Portion	ventral - dorsal	-3.30	0.29	-3.86	-2.74	181	-11.50	<.001

Moreover, Table 2 shows statistically significant main effects of the hemisphere, visual area, and the visual area portion on individual variability of eccentricity maps. Like polar angle maps, eccentricity maps of the left hemisphere show higher individual variability than those in the right hemisphere (mean difference = 0.14, p<.001). The dorsal portion of early visual areas is also more variable than the ventral portion (mean difference = 0.13, p<.001). For visual areas, post-hoc comparisons indicated that the only statistically significant difference was that of V3 versus V1, with V3 having higher individual variability than V1 (mean difference = 0.05, p<.004). In addition, statistically significant interactions were also found (Supplementary Material). Each visual area in the left hemisphere has significantly higher individual variability than analogous areas in the right hemisphere, except for V3. Eccentricity maps of each visual area's dorsal portion in the left hemisphere are significantly more variable than the dorsal

counterpart in the right hemisphere, and the ventral analogues in both the left and the right hemispheres.

Table 2 – Fixed effects parameters estimates for the linear mixed model of individual variability of eccentricity maps. SE – standard error; CI – confidence interval.

Eccentricity								
				95% CI				
Names	**Effect**	**Estimate**	**SE**	**Lower**	**Upper**	**df**	**t**	**p**
Intercept	Intercept	0.81	0.02	0.77	0.85	180	41.86	<.001
Hemisphere	RH-LH	-0.14	0.01	-0.16	-0.11	181	-10.91	<.001
Visual area (1)	V2-V1	0.01	0.01	-0.01	0.04	402	0.98	0.326
Visual area (2)	V3-V1	0.05	0.01	0.02	0.08	182	3.24	0.001
Portion	ventral - dorsal	-0.13	0.03	-0.18	-0.07	180	-4.64	<.001

Next, we performed an exploratory analysis to determine whether retinotopic maps differ from the average map in similar ways, particularly in the dorsal portion of early visual cortex of the left hemisphere. We focus on results for polar angle maps here as no meaningful differences were observed across eccentricity map clusters (Supplementary Figure 1). We computed the extent of overlap between discrete polar angle maps from all possible pairs of individuals using the Jaccard index, resulting in a similarity matrix (Figure 3a). Next, we applied a spectral clustering algorithm with a fixed number of clusters equal to 6 (Figure 3b). Finally, we averaged the continuous polar angle maps across individuals within each cluster to visualize common patterns of retinotopic organization in the dorsal portion of early visual cortex (Figure 3c).

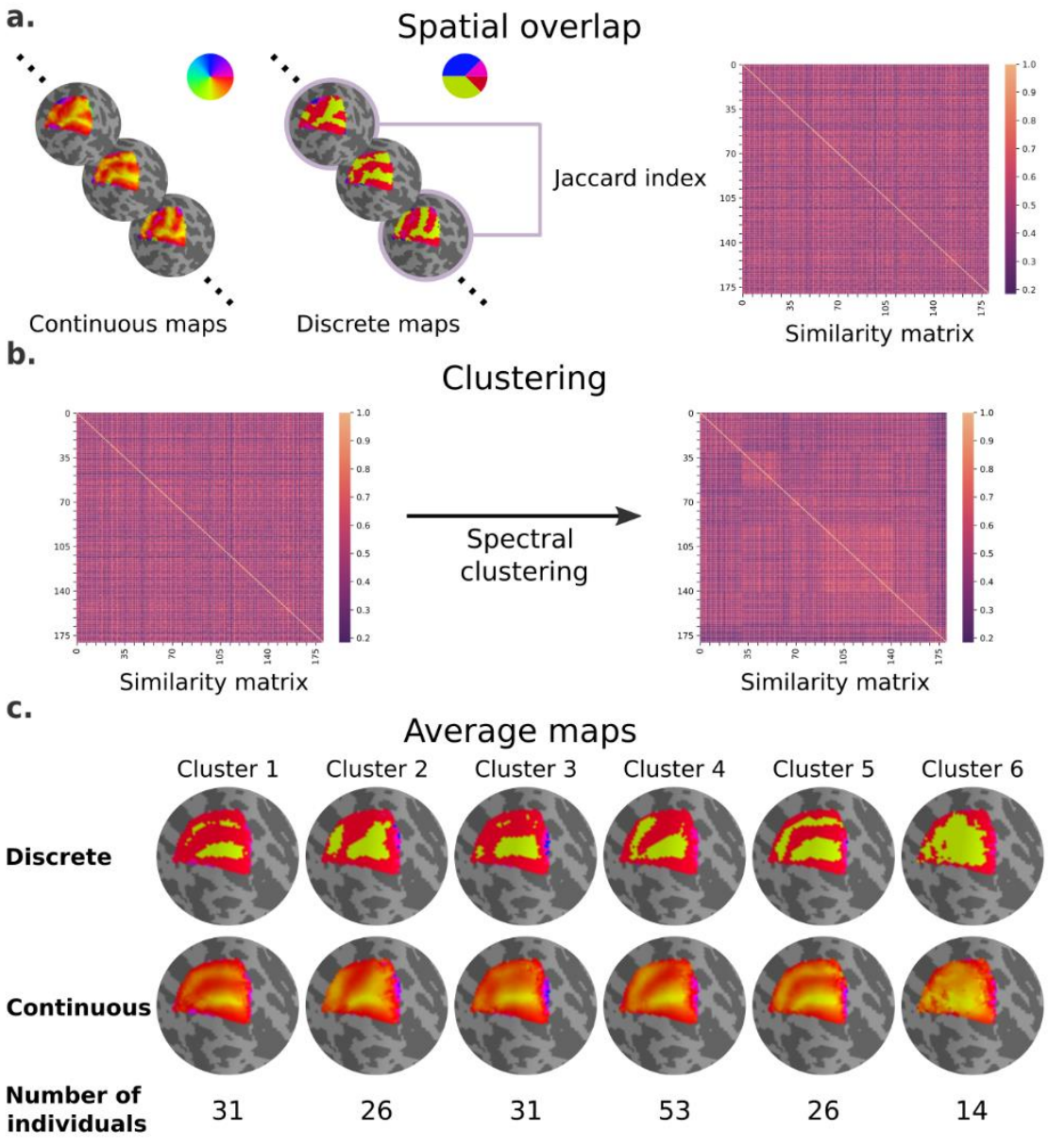

Figure 3 - Clusters of retinotopic organization in the dorsal portion of early visual cortex. a, Continuous polar angle maps were converted into discrete maps, such that each vertex would be categorized into one out of four possible labels. Spatial overlap between discrete maps was estimated using the Jaccard similarity coefficient from all possible pairs of individuals, resulting in a 181×181 similarity matrix. **b,** Then, we applied a spectral clustering algorithm – setting the number of clusters to 6. **c,** An average map (discrete and continuous) was calculated for each cluster by averaging the continuous polar angle maps across all individuals within each cluster.

Our findings clearly indicate shared patterns of retinotopic organization that deviate from the typical polar angle representation in the dorsal portion of early visual cortex

(Figure 1c). Specifically, average maps from clusters 1 and 5 capture nearly a third of individuals and show typical polar angle representations, with clear boundaries between V1/V2 and V2/V3 (Figure 1c and Figure 3c). However, clusters 2, 3, and 4 capture nearly two thirds of individuals and deviate from this typical polar angle representation (Figure 3c). The average map from cluster 2 shows that the boundaries between V1 and V2, and the most anterior portion of V3 and higher-order visual areas, merge to form a Y-shaped (or forked) lower vertical representation. Clusters 3 and 4 show a truncated V3 boundary, indicating that dorsal V3 does not cover the entire quarter visual field (i.e., from 360º to 270º) either throughout its length or only in its most anterior portion. Finally, cluster 6 reflects unclear retinotopic organization, with a handful of individuals' retinotopic maps showing overall low correspondence with the typical retinotopic organization.

Qualitatively, individual maps seem to agree with their corresponding average cluster map, but there are some exceptions (Figure 4, Supplementary Figure 2). Figure 4 shows the average cluster maps from each cluster and examples of individuals' maps that are qualitatively similar and dissimilar to their corresponding average cluster map. While most polar angle maps correspond well with their average cluster maps (as seen in the middle row of Figure 4), there is also an apparent mismatch between a few maps and their corresponding cluster average (bottom row in Figure 4). For example, individual #132118 was assigned to Cluster 4, but their polar angle map is qualitatively more similar to Cluster 5. These mismatches are likely due to the extensive overlap between within-cluster and between-clusters distributions of pairwise Jaccard scores (Figure 5). Note in Figure 5 that the within-cluster distributions highlighted in grey are generally shifted to the right compared to the between-clusters distributions, indicating their higher Jaccard scores. However, the overlap between these distributions is

substantial. For example, the between cluster 1 and 5 distribution overlaps with within-cluster 1 distribution throughout its entirety, which is justified by the significant similarity between their average maps. Despite this, we found that the average within-cluster Jaccard score is 0.54 (SD = 0.07), while the average between-clusters score is 0.46 (SD = .08), showing that pairs of maps within a cluster are, on average, more similar than between-clusters.

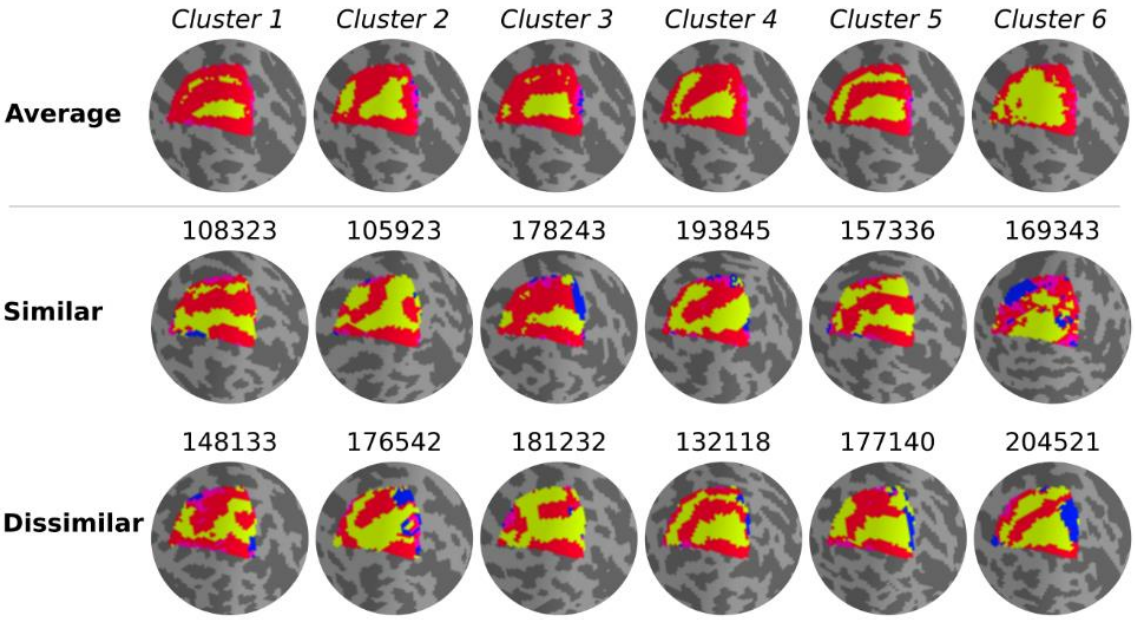

Figure 4 - Qualitative evaluation of clusters. Average cluster maps are shown in the top row. The middle row shows examples of maps from each cluster with a similar retinotopic organization to the corresponding average map. Finally, in the bottom row, examples of those with dissimilar organizations are shown.

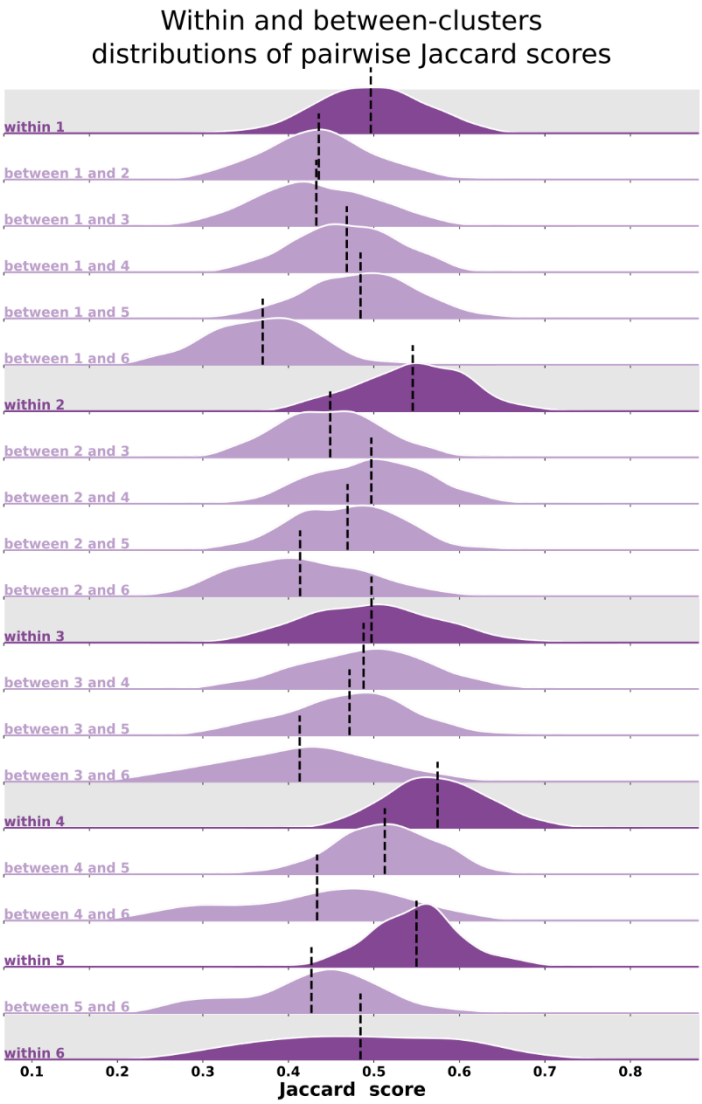

Figure 5 - Distributions of pairwise Jaccard scores. Within and between-clusters distribution of Jaccard scores across all pairs of individuals. Within-cluster distributions are highlighted in grey. Between-clusters distributions are the same regardless of the order of the clusters, i.e., the Jaccard score distribution between cluster 1 and cluster 2 ('between 1 and 2') is the same as the one between cluster 2 and 1. Black vertical lines indicate distributions' means.

Discussion

We systematically investigated individual variability in visual field representation of human early visual cortex using the HCP 7T retinotopy dataset. We found that retinotopic maps in the left hemisphere were more variable than those in the right

hemisphere. Moreover, in the left hemisphere the dorsal portions of early visual areas were more variable than their ventral counterparts. Additionally, we investigated whether there are common motifs in the observed individual variability in retinotopic maps. This analysis showed that deviations from the canonical model of continuous, alternating bands of vertical and horizontal meridian representation in V2 and V3 exist in the majority of individuals. Overall, our findings challenge the current view that the dorsal portions of early visual areas form retinotopic maps which are consistent between individuals as roughly mirror images of their ventral counterparts.

Although previous evidence for the variability seen across dorsal early visual cortex in humans has been mostly anecdotal, a number of studies have indicated a complex, retinotopic organization of dorsal early visual areas in non-human primates, using both electrophysiological recordings and high-resolution fMRI (Angelucci and Rosa, 2015; Gattass et al., 1988; Sereno et al., 2015; Zhu and Vanduffel, 2019). Accordingly, there is a long-standing debate about the number of visual areas – and their boundaries – in the third-tier visual cortex of New and Old-World monkeys (Angelucci and Rosa, 2015; Hadjidimitrakis et al., 2019). However, the question of whether the areal boundaries in this region show significant individual variability has not been studied systematically in non-human primates. Only Gattass et al. (1988) reported, in the macaque monkey, that the representation of the lower vertical meridian in dorsal V3 varied across individuals, but firm conclusions could not be drawn due to the small sample. These authors indicated that some animals showed a continuous representation of this meridian along the rostral border of this area, whereas in others additional field discontinuities created a discontinuous representation. Notably, the same discontinuities in the anterior border of dorsal V3 were also found in our systematic investigation of individual variability in human polar angle maps. It is also

389 significant that the same pattern of variation (relatively simple and reproducible
390 representations of the upper contralateral quadrant, and complex and variable
391 representations of the lower quadrant) characterize V2 and V3 in at least one non-
392 primate, the cat (Rosa and Manger, 2005; Tusa et al., 1979). Overall, our findings in
393 humans demonstrate that the organization of dorsal early visual areas is more
394 heterogeneous than previously acknowledged and suggest that this may be a common
395 feature of mammals with developed vision.

396 Although different models of third-tier visual cortex organization in non-human
397 primates (Angelucci and Rosa, 2015) also suggest unusual eccentricity mapping, we
398 did not find meaningful differences in clusters of eccentricity maps. This may be
399 associated with the limited extent of the visual stimulus (up to 8° of eccentricity)
400 (Benson et al., 2018) and remains to be further investigated. Another alternative is
401 having a complex pattern of polar angle representation coexisting with a preserved
402 eccentricity gradient, as demonstrated by previous work in areas V2 and V3 of cats
403 (Tusa et al., 1979), flying foxes (Rosa, 1999), ferrets (Manger et al., 2002) and tree
404 shrews (Sedigh-Sarvestani et al., 2021).

405 Our investigation provides firm evidence for individual variability in the retinotopic
406 organization across parts of early visual areas in the human visual cortex. Moreover,
407 the exploratory analysis indicates the presence of shared patterns of retinotopic
408 organization that deviate from the typical polar angle representation in the dorsal
409 portion of early visual cortex. Future work could extend these insights through
410 additional analyses – for example, by employing different similarity metrics, using
411 different features, or changing the number of clusters. Here, we limited our analysis to
412 the spatial overlap of discrete polar angle maps, which means that a pair of
413 qualitatively similar but spatially misaligned polar angle maps, for example, might have

a low Jaccard score. If another more suitable metric can consider the topographic organization of polar angle maps regardless of the spatial location, it would be possible to increase the consistency between an individual's map and their cluster average map. It would also be possible to estimate the similarity between two individuals' retinotopic maps from specific features extracted from the maps (such as linear magnification along isoeccentricity lines), to provide insights into changes in these properties as a function of cortical location (Schira et al., 2010). Finally, it is important to note that selecting the ideal number of clusters depends on the similarity metric employed, prior knowledge, and the clustering algorithm. Therefore, future work could be performed to explore the effect of the number of clusters on clustering quality (perhaps as indicated by within- vs. between-cluster similarity measures).

Given the presence of the variability across early visual cortex in humans, another potential line of investigation involves the origin of this variability. Pertinently, we recently developed a deep learning model of retinotopy able to predict this individual variability from individual-specific cortical curvature and myelin maps (Ribeiro et al., 2021), suggesting that it is a structure-related variation. In our subsequent work (Ribeiro et al., 2022), we further explored this model of retinotopy to unravel which anatomical feature (curvature or myelin) was the most important for individual variability in the dorsal portion of early visual cortex. Although we found neither feature was redundant, the model seems to be differentially relying on myelin feature maps to determine individual variability in the dorsal portion of early visual cortex. Studies modelling the formation of retinotopic maps in development have suggested that multistable solutions may occur depending on factors such as the degree of elongation of the area (Sedigh-Sarvestani et al., 2021; Wolf et al., 1994) and adjacency with other areas (Yu et al., 2020), which do not violate the need to minimize the length of

connections (Durbin and Mitchison, 1990; Swindale, 1996). Therefore, future work could evaluate whether there is an overlap between function- and anatomy-based clusters to help elucidate the developmental mechanisms underlying the variability of human dorsal extrastriate cortex.

Finally, another finding that requires consideration is the interhemispheric difference revealed in our data: retinotopic maps in the left hemisphere showed more variation than those in the right hemisphere. To date, there has been no report of interhemispheric differences in early visual cortex of other mammals, including non-human primates. In part, this may be traced to the relatively small samples in these studies, in comparison with those possible using human fMRI. However, another possibility is that such differences may arise more frequently in human brains, due to the scaling of callosal connections with brain size (Rilling and Insel, 1999), which may promote a higher degree of connectional independence during development.

In conclusion, using a large-scale brain imaging dataset, we provide new insights into the variability in the topographical organization of human visual cortex. These insights may prove crucial in guiding further experimental investigations and theories about retinotopic organization differentiation across species, development, and individuals.

Acknowledgments

This work was supported by the Australian Research Council (DE180100433 and DP210101042). Data were provided by the Human Connectome Project, WU-Minn Consortium (Principal Investigators: David Van Essen and Kamil Ugurbil; 1U54MH091657) funded by the 16 NIH Institutes and Centers that support the NIH Blueprint for Neuroscience Research; and by the McDonnell Center for Systems

462 Neuroscience at Washington University. In addition, FLR acknowledges support
463 through the Australian Government Research Training Program Scholarship.

464 **Competing financial interests**

465 The authors declare no competing financial interests.

466 **References**

467 Abraham, A., Pedregosa, F., Eickenberg, M., Gervais, P., Mueller, A., Kossaifi, J.,
468 Gramfort, A., Thirion, B., Varoquaux, G., 2014. Machine learning for neuroimaging
469 with scikit-learn. Front. Neuroinform. 8, 1–10.
470 https://doi.org/10.3389/fninf.2014.00014

471 Allen, E.J., St-Yves, G., Wu, Y., Breedlove, J.L., Prince, J.S., Dowdle, L.T., Nau, M.,
472 Caron, B., Pestilli, F., Charest, I., Hutchinson, J.B., Naselaris, T., Kay, K., 2021.
473 A massive 7T fMRI dataset to bridge cognitive neuroscience and artificial
474 intelligence. Nat. Neurosci. https://doi.org/10.1038/s41593-021-00962-x

475 Angelucci, A., Rosa, M.G.P., 2015. Resolving the organization of the third tier visual
476 cortex in primates: A hypothesis-based approach. Vis. Neurosci. 32.
477 https://doi.org/10.1017/S0952523815000073

478 Arcaro, M.J., Kastner, S., 2015. Topographic organization of areas V3 and V4 and its
479 relation to supra-areal organization of the primate visual system. Vis. Neurosci.
480 https://doi.org/doi:10.1017/S0952523815000115

481 Benson, N.C., Butt, O.H., Brainard, D.H., Aguirre, G.K., 2014. Correction of Distortion
482 in Flattened Representations of the Cortical Surface Allows Prediction of V1-V3
483 Functional Organization from Anatomy. PLoS Comput. Biol. 10.

https://doi.org/10.1371/journal.pcbi.1003538

Benson, N.C., Butt, O.H., Datta, R., Radoeva, P.D., Brainard, D.H., Aguirre, G.K., 2012. The retinotopic organization of striate cortex is well predicted by surface topology. Curr. Biol. 22, 2081–2085. https://doi.org/10.1016/j.cub.2012.09.014

Benson, N.C., Jamison, K.W., Arcaro, M.J., Vu, A.T., Glasser, M.F., Coalson, T.S., Van Essen, D.C., Yacoub, E., Ugurbil, K., Winawer, J., Kay, K., 2018. The Human Connectome Project 7 Tesla retinotopy dataset : Description and population receptive field analysis. J. Vis. 18, 1–22.

Benson, N.C., Winawer, J., 2018. Bayesian analysis of retinotopic maps. Elife 7, 1–29. https://doi.org/10.7554/elife.40224

Dumoulin, S.O., Wandell, B.A., 2008. Population receptive field estimates in human visual cortex. Neuroimage 39, 647–660. https://doi.org/10.1016/j.neuroimage.2007.09.034

Durbin, R., Mitchison, G., 1990. A dimension reduction framework. Nature 343, 644–647.

Gattass, R., Gross, C.G., Sandell, J.H., 1981. Visual topography of V2 in the macaque. J. Comp. Neurol. 201, 519–539. https://doi.org/10.1002/cne.902010405

Gattass, R., Sousa, A.P.B., Gross, C.G., 1988. Visuotopic organization and extent of V3 and V4 of the macaque. J. Neurosci. 8, 1831–1845. https://doi.org/10.1523/jneurosci.08-06-01831.1988

Glasser, M.F., Coalson, T.S., Robinson, E.C., Hacker, C.D., Harwell, J., Yacoub, E., 2016. A multi-modal parcellation of human cerebral cortex. Nature 536, 171–178. https://doi.org/10.1038/nature18933

507 Glasser, M.F., Sotiropoulos, S.N., Wilson, J.A., Coalson, T.S., Fischl, B., Andersson,
508 J.L., Xu, J., Jbabdi, S., Webster, M., Polimeni, J.R., Van Essen, D.C., Jenkinson,
509 M., 2013. The minimal preprocessing pipelines for the Human Connectome
510 Project. Neuroimage 80, 105–124.
511 https://doi.org/10.1016/j.neuroimage.2013.04.127

512 Hadjidimitrakis, K., Bakola, S., Chaplin, T.A., Yu, H.H., Alanazi, O., Chan, J.M.,
513 Worthy, K.H., Rosa, M.G.P., 2019. Topographic organization of the 'third-tier'
514 dorsomedial visual cortex in the macaque. J. Neurosci. 39, 5311–5325.
515 https://doi.org/10.1523/JNEUROSCI.0085-19.2019

516 Kay, K.N., Winawer, J., Mezer, A., Wandell, B.A., 2013. Compressive spatial
517 summation in human visual cortex. J. Neurophysiol. 110, 481–494.
518 https://doi.org/10.1152/jn.00105.2013

519 Levandowsky, M., Winter, D., 1971. Distance between sets. Nature 234, 34–35.
520 https://doi.org/10.1038/234034a0

521 Luxburg, U. Von, 2007. A tutorial on spectral clustering. Stat. Comput. 17, 395–416.
522 https://doi.org/10.1007/s11222-007-9033-z

523 Magezi, D.A., 2015. Linear mixed-effects models for within-participant psychology
524 experiments: An introductory tutorial and free, graphical user interface (LMMgui).
525 Front. Psychol. 6, 1–7. https://doi.org/10.3389/fpsyg.2015.00002

526 Manger, P.R., Kiper, D., Masiello, I., Murillo, L., Tettoni, L., Hunyadi, Z., Innocenti,
527 G.M., 2002. The Representation of the Visual Field in Three Extrastriate Areas of
528 the Ferret (Mustela putorius) and the Relationship of Retinotopy and Field
529 Boundaries to Callosal Connectivity. Cereb. Cortex 12, 423–437.
530 https://doi.org/10.1093/cercor/12.4.423

Pedregosa, F., Varoquaux, G., Gramfort, A., Michel, V., Thirion, B., Grisel, O., Blondel, M., Prettenhofer, P., Weiss, R., Dubourg, V., Vanderplas, J., Passos, A., Cournapeau, D., Brucher, M., Perrot, M., Duchesnay, E., 2011. Scikit-learn: Machine Learning in Python. J. Mach. Learn. Res. 12, 2825–2830.

Ribeiro, F.L., Bollmann, S., Cunnington, R., Puckett, A.M., 2022. An explainability framework for cortical surface-based deep learning. arXiv 1–10.

Ribeiro, F.L., Bollmann, S., Puckett, A.M., 2021. Predicting the retinotopic organization of human visual cortex from anatomy using geometric deep learning. Neuroimage 244, 118624. https://doi.org/https://doi.org/10.1016/j.neuroimage.2021.118624

Rilling, J.K., Insel, T.R., 1999. Differential expansion of neural projection systems in primate brain evolution. Neuroreport 10, 1453–1459. https://doi.org/10.1097/00001756-199905140-00012

Rosa, M.G.P., 2002. Visual maps in the adult primate cerebral cortex: some implications for brain development and evolution. Brazilian J. Med. Biol. Res. 35, 1485–1498. https://doi.org/10.1590/S0100-879X2002001200008

Rosa, M.G.P., 1999. Topographic organisation of extrastriate areas in the flying fox: Implications for the evolution of mammalian visual cortex. J. Comp. Neurol. 411, 503–523. https://doi.org/10.1002/(SICI)1096-9861(19990830)411:3<503::AID-CNE12>3.0.CO;2-6

Rosa, M.G.P., Manger, P.R., 2005. Clarifying homologies in the mammalian cerebral cortex: The case of the third visual area (V3). Clin. Exp. Pharmacol. Physiol. 32, 327–339. https://doi.org/10.1111/j.1440-1681.2005.04192.x

Schira, M.M., Tyler, C.W., Breakspear, M., Spehar, B., 2009. The foveal confluence in

554 human visual cortex. J. Neurosci. 29, 9050–9058.
555 https://doi.org/10.1523/JNEUROSCI.1760-09.2009

556 Schira, M.M., Tyler, C.W., Spehar, B., Breakspear, M., 2010. Modeling magnification
557 and anisotropy in the primate foveal confluence. PLoS Comput. Biol. 6, 1–10.
558 https://doi.org/10.1371/journal.pcbi.1000651

559 Sedigh-Sarvestani, M., Lee, K.-S., Jaepel, J., Satterfield, R., Shultz, N., Fitzpatrick, D.,
560 2021. A sinusoidal transformation of the visual field is the basis for periodic maps
561 in area V2. Neuron 109, 4068-4079.e6.
562 https://doi.org/10.1016/j.neuron.2021.09.053

563 Sereno, M.I., McDonald, C.T., Allman, J.M., 2015. Retinotopic organization of
564 extrastriate cortex in the owl monkey—dorsal and lateral areas. Vis. Neurosci. 32,
565 E021. https://doi.org/10.1017/S0952523815000206

566 Swindale, N. V, 1996. The development of topography in the visual cortex: a review of
567 models. Network 7, 161–247. https://doi.org/10.1088/0954-898X/7/2/002

568 Taha, A.A., Hanbury, A., 2015. Metrics for evaluating 3D medical image segmentation:
569 Analysis, selection, and tool. BMC Med. Imaging 15.
570 https://doi.org/10.1186/s12880-015-0068-x

571 The jamovi project (2021), n.d.

572 Tusa, R.J., Rosenquist, A.C., Palmer, L.A., 1979. Retinotopic organization of areas 18
573 and 19 in the cat. J. Comp. Neurol. 185, 657–678.
574 https://doi.org/10.1002/cne.901850405

575 Van Essen, D.C., Glasser, M.F., 2018. Parcellating Cerebral Cortex: How Invasive
576 Animal Studies Inform Noninvasive Mapmaking in Humans. Neuron 99, 640–663.

https://doi.org/10.1016/j.neuron.2018.07.002

Van Essen, D.C., Smith, S.M., Barch, D.M., Behrens, T.E.J., Yacoub, E., Ugurbil, K., 2013. The WU-Minn Human Connectome Project: An overview. Neuroimage 80, 62–79. https://doi.org/10.1016/j.neuroimage.2013.05.041

Wandell, B.A., Winawer, J., 2010. Imaging retinotopic maps in the human brain. Vision Res. 51, 718–737. https://doi.org/10.1016/j.visres.2010.08.004.Imaging

Wang, L., Mruczek, R.E.B., Arcaro, M.J., Kastner, S., 2015. Probabilistic maps of visual topography in human cortex. Cereb. Cortex 25, 3911–3931. https://doi.org/10.1093/cercor/bhu277

Wolf, F., Bauer, H.U., Geisel, T., 1994. Formation of field discontinuities and islands in visual cortical maps. Biol. Cybern. 70, 525–531. https://doi.org/10.1007/BF00198805

Yu, H.H., Rowley, D.P., Price, N.S.C., Rosa, M.G.P., Zavitz, E., 2020. A twisted visual field map in the primate cortex predicted by topographic continuity. Sci. Adv. https://doi.org/10.1101/682187

Yu, Z., Guindani, M., Grieco, S.F., Chen, L., Holmes, T.C., Xu, X., 2022. Primer Beyond t test and ANOVA : applications of mixed-effects models for more rigorous statistical analysis in neuroscience research. Neuron 110, 21–35. https://doi.org/10.1016/j.neuron.2021.10.030

Zhu, Q., Vanduffel, W., 2019. Submillimeter fMRI reveals a layout of dorsal visual cortex in macaques, remarkably similar to New World monkeys. Proc. Natl. Acad. Sci. U. S. A. 116, 2306–2311. https://doi.org/10.1073/pnas.1805561116